


Article

Synergistic Effects of 1-Octyl-3-Methylimidazolium Hexafluorophosphate and Cellulose Nanocrystals on Improving Polyacrylate Waterborne Anti-Corrosion Coatings

Zeping Wang ¹, Binjie Hu ^{1,*}, Haibin Yu ² and George Zheng Chen ³ 

¹ Key Laboratory of Carbonaceous Wastes Processing and Process Intensification of Zhejiang Province, Department of Chemical & Environmental Engineering, University of Nottingham Ningbo China, 199 Taikang East Road, Ningbo 315000, China

² Ningbo Institute of Materials Technology and Engineering, Chinese Academy of Sciences, Ningbo 315201, China

³ Department of Chemical and Environmental Engineering, Advanced Materials Research Group, Faculty of Engineering, University of Nottingham, Nottingham NG7 2RD, UK

* Correspondence: binjie.hu@nottingham.edu.cn

Abstract: In this study, three copolymers of poly(methyl methacrylate) and poly(butyl acrylate) (PMMA-co-PBA) latex containing 1-octyl-3 methylimidazolium hexafluorophosphate (C_8mimPF_6), cellulose nanocrystals (CNCs), and C_8mimPF_6 -CNCs were successfully synthesized through mini emulsion polymerization. These novel composites were each coated on mild steel panels and tested for their anti-corrosion performance by immersion of the coated samples in 3.5 wt% sodium chloride (NaCl) solution over a certain period. The synergistic anti-corrosion effects of the C_8mimPF_6 -CNCs sample led to the highest coating resistance, charge transfer resistance, and corrosion inhibition efficiency and the lowest diffusion coefficient and corrosion rate. The proposed synergistic mechanism revealed that CNCs enhanced the barrier effect of the coating while C_8mimPF_6 inhibited corrosion when released.

Keywords: ionic liquid; cellulose nanocrystals; corrosion protection; polymer; electrochemical analysis; composite



Citation: Wang, Z.; Hu, B.; Yu, H.; Chen, G.Z. Synergistic Effects of 1-Octyl-3-Methylimidazolium Hexafluorophosphate and Cellulose Nanocrystals on Improving Polyacrylate Waterborne Anti-Corrosion Coatings. *Polymers* **2023**, *15*, 810. <https://doi.org/10.3390/polym15040810>

Academic Editor: Yujie Qiang

Received: 25 December 2022

Revised: 1 February 2023

Accepted: 2 February 2023

Published: 6 February 2023



Copyright: © 2023 by the authors. Licensee MDPI, Basel, Switzerland. This article is an open access article distributed under the terms and conditions of the Creative Commons Attribution (CC BY) license (<https://creativecommons.org/licenses/by/4.0/>).

1. Introduction

The ionic liquid C_8mimPF_6 as a corrosion inhibitor has been proven to be effective in waterborne anti-corrosion coatings on mild steel in simulated seawater, i.e., 3.5 wt% NaCl solution [1]. The mechanism of C_8mimPF_6 in corrosion inhibition is mainly ascribed to the adsorption of imidazolium ions to passivate the reaction sites on the metal surface, which in turn prevents corrosion from occurring when encapsulated C_8mimPF_6 is released into the corrosive medium [1,2]. Although the anti-corrosion performance was enhanced with the introduction of C_8mimPF_6 , it was still inferior to other anti-corrosion coatings, such as epoxy, due to the poor performance of neat waterborne PMMA-co-PBA [3]. However, as one of the acrylate coatings, waterborne PMMA-co-PBA coatings have advantages such as low cost, excellent adhesion, coalescence, color retention, and satisfactory UV and hydrolysis resistance [4,5]. Rather than searching for alternative waterborne coating resins without prior anti-corrosion resistance to encapsulate C_8mimPF_6 , direct addition of fillers to enhance the barrier effect of the neat PMMA-co-PBA coating is a facile route to improve the anti-corrosion performance [6].

Cellulose, a natural filler, is fibrous, tough, water-insoluble, biodegradable, biocompatible, renewable polymer, and is also abundant in nature [7]. Cellulose can form nanocrystals (CNCs) which, unlike cellulose nanofibers (CNFs) with highly entangled web-like structures, present shorter lengths and needle-like shapes [8]. Hydroxyl groups in CNCs lead to strong hydrogen bonds and a highly crystalline structure [7]. Moreover, CNCs can act as a

gas or water-impermeable barrier and additives can enhance the mechanical properties of coatings [9,10]. He et al. [11] incorporated CNCs into a waterborne acrylate coating and compared the anti-corrosion performance before and after CNC addition. They found that the polarization resistance of the coating with CNCs slightly increased after 35 days of exposure, whilst the water uptake was relatively stable at a low level. On the contrary, the polar resistance of the coating without CNCs decreased after 21 days of exposure, with the coating showing remarkable degradation. They ascribed the enhancement effect to hydrogen bonding between CNCs and other coating materials. Therefore, we are interested to introduce CNCs as fillers into our previously reported ionic liquid-containing anti-corrosion coating formula [1]. Previous reports have shown that iridescent PVA composite films can be fabricated with the combination of CNCs and ionic liquids [12]. This composite is of high strength and toughness [13] and can adsorb and recover lithium ions from groundwater [14]. These works reveal that CNCs and ionic liquid could be homogenized in one functioning composite. So far, no research work has reported such an idea to combine C_8mimPF_6 and CNCs into a waterborne acrylate coating. To the best of our knowledge, we are the first to incorporate C_8mimPF_6 and CNCs as a corrosion inhibitor and barrier into coating fillers. In this research, systematic characterizations and analyses on the anti-corrosion performance were carried out, exploring their synergistic effect and the underlying anti-corrosion mechanism.

2. Materials and Experimental Methods

2.1. Materials

Methyl methacrylate (MMA, CP), sodium dodecyl sulfonate (SDSO, CP), L-Ascorbic acid (AAc, AR), and hydrogen peroxide (H_2O_2 , AR) were purchased from Sinopharm Chemical Reagent Co., Ltd, Shanghai, China. Hexadecane (HD, 98%) and n-butyl acrylate (BA, 99%) were purchased from Aladdin Industrial Inc, Shanghai, China. Cellulose nanocrystals (CNCs) were kindly supplied by ScienceK Co., Ltd, Huzhou, China. The compound 1-octyl-3 methylimidazolium hexafluorophosphate (C_8mimPF_6 , 99%) was purchased from Cheng Jie Chemical Co., Ltd, Shanghai, China. Ultra-pure water with a resistivity of less than $18.2 M\Omega\text{ cm}$ was used in all experiments. A mild steel panel (steel Q235) for testing was bought from Zhi Bao Metal Products Co., Ltd, Shenzhen, China. The mild steel composition (wt%) was 0.14–0.22 C, 0.3–0.65 Mn, < 0.30 Si, < 0.045 p, < 0.055 S, and the remaining was Fe.

2.2. Preparation of Mini Emulsion

The mini emulsion was prepared by mixing the oil phase containing a 1:1 mass ratio of MMA to BA. C_8mimPF_6 (10 wt%) and 0.5 wt% CNC were added to the oil and water phase, respectively, before phase mixing. A sonicator (Scientz II, Xinzhi Co., Ltd, Ningbo, China) was used to homogenize the two-phase mixture using a power of 285 W for 6 min with a pattern of 1 s on and 1 s off.

2.3. Mini Emulsion Polymerization

Polymerization was carried out in a 250 mL four-necked flask equipped with a stirrer, a reflux condenser, a thermometer, and a nitrogen inlet. The flask was immersed in a water bath with the temperature controlled at $40\text{ }^\circ\text{C}$. The mini emulsion was loaded into the flask and stored under stirring and nitrogen bubbling for 1.5 h to remove oxygen. After the reaction temperature ($40\text{ }^\circ\text{C}$) was reached, a 0.1 mol% H_2O_2 /AAc solution with a molar ratio of 1 to 1.3 was injected to start the reaction.

2.4. Coating Film Characterization

2.4.1. Testing Sample Preparation

Before characterization, the copolymer coating film was prepared as follows. After treatment with emery paper, mild steel specimens of 1 cm in length and 1 cm in width were selected as the substrate for coating. After treatment with emery paper, several drops of

latex developed in previous steps were dropped onto one side of the surface of the mild steel specimen, followed by the rolling of bar coater BGD212/150 μm from one side to the other side evenly. After evaporation of water, the solid content remained. The thickness of the film was measured with a PosiTectorFS1 apparatus, and the film thickness was controlled at $40 \pm 2 \mu\text{m}$.

2.4.2. FTIR

FTIR spectra of copolymer coating samples were collected using Vertex 70, Bruker Co., Ltd, Beilin, Germany. The operation was carried out over the wavenumber range of 4000 to 400 cm^{-1} with a resolution of 4 cm^{-1} .

2.4.3. Surface Morphology

The surface morphology of the coating film was investigated by a scanning electron microscope (SEM) (Σ IGMA/VP, Carl Zeiss Microscopy Ltd., Jena, Germany) at an accelerating voltage of 4 kV.

2.4.4. Wettability

The contact angle between water and the coated mild steel surface was measured with a dynamic contact angle measuring instrument (Theta Flex, Biolin Scientific Co Ltd., Shanghai, China). Initially, 5 μL of water droplets was loaded on the tip of a needle tube, and after dropping onto the coated mild steel surface, the contact angle was recorded at the 20th second. The contact angle measurements were repeated three times for each sample. An average value was used for the final measurement result.

2.4.5. Electrochemical Techniques

The anti-corrosion performances of the coatings were measured using Princeton's electrochemical workstation. A conventional three-electrode configuration electrochemical cell was prepared with a volume of 30 mL. The mild steel electrode, a platinum sheet, an Ag/AgCl electrode (in 3.0 M KCl), and 3.5 wt% NaCl (aqueous) were used as the working, counter, and reference electrodes and the electrolyte, respectively. The open circuit potential (OCP) for each sample was measured for 0.5 h before electrochemical impedance spectroscopy (EIS) and potentiodynamic polarization curves were measured. The EIS test was performed at the OCP with a frequency range of 10 kHz to 10 mHz under $\pm 10 \text{ mV}$ amplitude sinusoidal voltage. Tafel plots were scanned at rate of 0.5 mV/s in the range of $\pm 250 \text{ mV VS.OCP}$.

3. Results and Discussion

The latex was prepared as described in Section 2.3. The anti-corrosion performances of the copolymer coatings containing C_8mimPF_6 and CNCs were evaluated via open circuit potential (OCP), electrochemical impedance spectroscopy (EIS), and Tafel polarization curves. The status of C_8mimPF_6 and CNCs was revealed, and the mechanism of the synergistic effect was further explained in the following sections.

3.1. Anti-Corrosion Performance Evaluation of Copolymer Coating

3.1.1. Open Circuit Potential (OCP)

The electrochemical technique started with open circuit potential (OCP) measurement. OCP indicates the thermodynamic tendency of a material under electrochemical oxidation in a corrosive medium [15]. In other words, OCP values can reflect the extent of corrosion. Severe corrosion exhibits a more negative OCP. The variation in OCP versus immersion time in the absence and presence of C_8mimPF_6 and CNCs is displayed in Figure 1. At the initial immersion stage, the OCP of bare (no coating layer), blank (with a neat PMMA-co-PBA coating), C_8mimPF_6 (PMMA-co-PBA coating with 10 wt% C_8mimPF_6), CNCs (PMMA-co-PBA coating with 0.5 wt% CNCs), and C_8mimPF_6 -CNCs (PMMA-co-PBA coating with 10 wt% C_8mimPF_6 and 0.5 wt% CNCs) samples were approximately -550 , -496 , -412 ,

−432, and −357 mV, respectively. The drop in OCP in the first 2 h was ascribed to the penetration of corrosive ions such as OH^- and Cl^- and oxygen through coating micropores and the coating/steel interface [16]. After 96 h of immersion, the OCP of bare mild steel reduced sharply from −550 mV to −645 mV, which indicated that bare mild steel was severely corroded. In addition, the OCP of blank, C_8mimPF_6 , CNCs, and $\text{C}_8\text{mimPF}_6\text{-CNCs}$ samples at 96 h were −605, −538, −556, and −457 mV, respectively. The steady OCP values of these samples from 48 h to 96 h was attributed to the saturated water absorption of the coating and the accumulation of corrosion products [17]. Among them, the lowest rate of decline was observed in the $\text{C}_8\text{mimPF}_6\text{-CNCs}$ sample. Thus, it could be concluded that the $\text{C}_8\text{mimPF}_6\text{-CNCs}$ sample exhibited the most pronounced anti-corrosive effect.

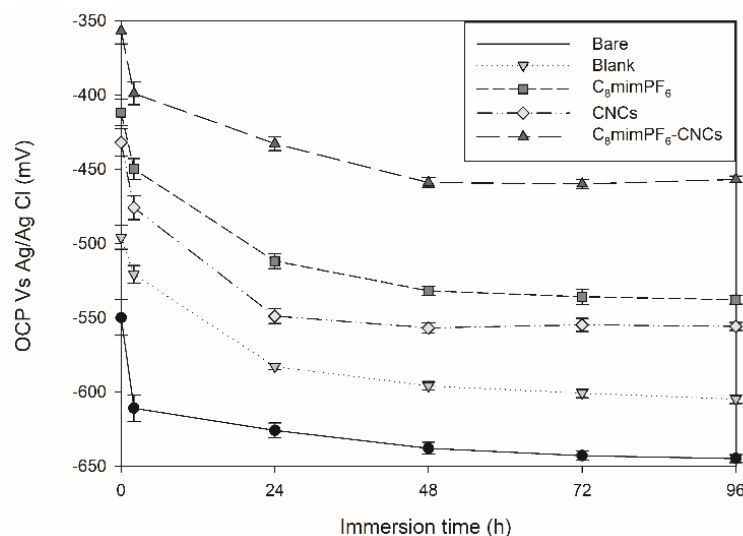


Figure 1. OCP for various samples at different immersion times.

3.1.2. Electrochemical Impedance Spectroscopy (EIS)

After the stabilization of OCP, other electrochemical techniques such as EIS and Tafel were applied to further quantitatively evaluate the extent of corrosion. For EIS, the resistance and capacitance of the coating could be directly obtained through data fitting. Moreover, with the obtained coating capacitance values, other indirect parameters such as the water absorption ratio of the coating and the diffusion coefficient of the corrosive ions could be calculated via the Brasher and Kingsbury equation [18] and the simplified Fick's law of diffusion [3], respectively.

Figure 2 shows the Nyquist impedance plots of different coated samples after 96 h of immersion in 3.5 wt% NaCl solution. The Nyquist plot is one of the manifestations of EIS tests, with different parts representing different hierarchies of the coating. For instance, in Figure 2a, the bottom left part at high frequency was correlated to defects and pinholes of the coating, while the upper right part at low frequency was assigned to the interface of the coating and the mild steel surface [19,20]. The shrinking semicircles during the immersion test exhibit the declining anti-corrosion performance. The initial linear portion of the curve shown in Figure 2c could be attributed to the pseudo-two-time constant phenomenon caused by the penetration of electrolytes through the coating defects [21,22]. Moreover, an electrical equivalent circuit was applied to model Nyquist plots for quantitative evaluation. As shown in Figure 3, the circuits consisted of different electrochemical parameters such as solution resistance (R_s), coating resistance (R_C), coating capacitance (C_C), charge transfer resistance (R_{ct}), and constant phase element (CPE_{dl}), where CPE_{dl} represents the non-ideal capacitance of double layer. Here, CPE is a valid model to simulate the dielectric response, which symbolizes a real-life capacitive impedance independent of frequency [23]. Using ZSimpWin 3.60 software, the results of resistance and capacitance were fitted and presented in Figure 4. Figure 4a and c show the coating resistance (R_C) and charge transfer resistance (R_{ct}), respectively.

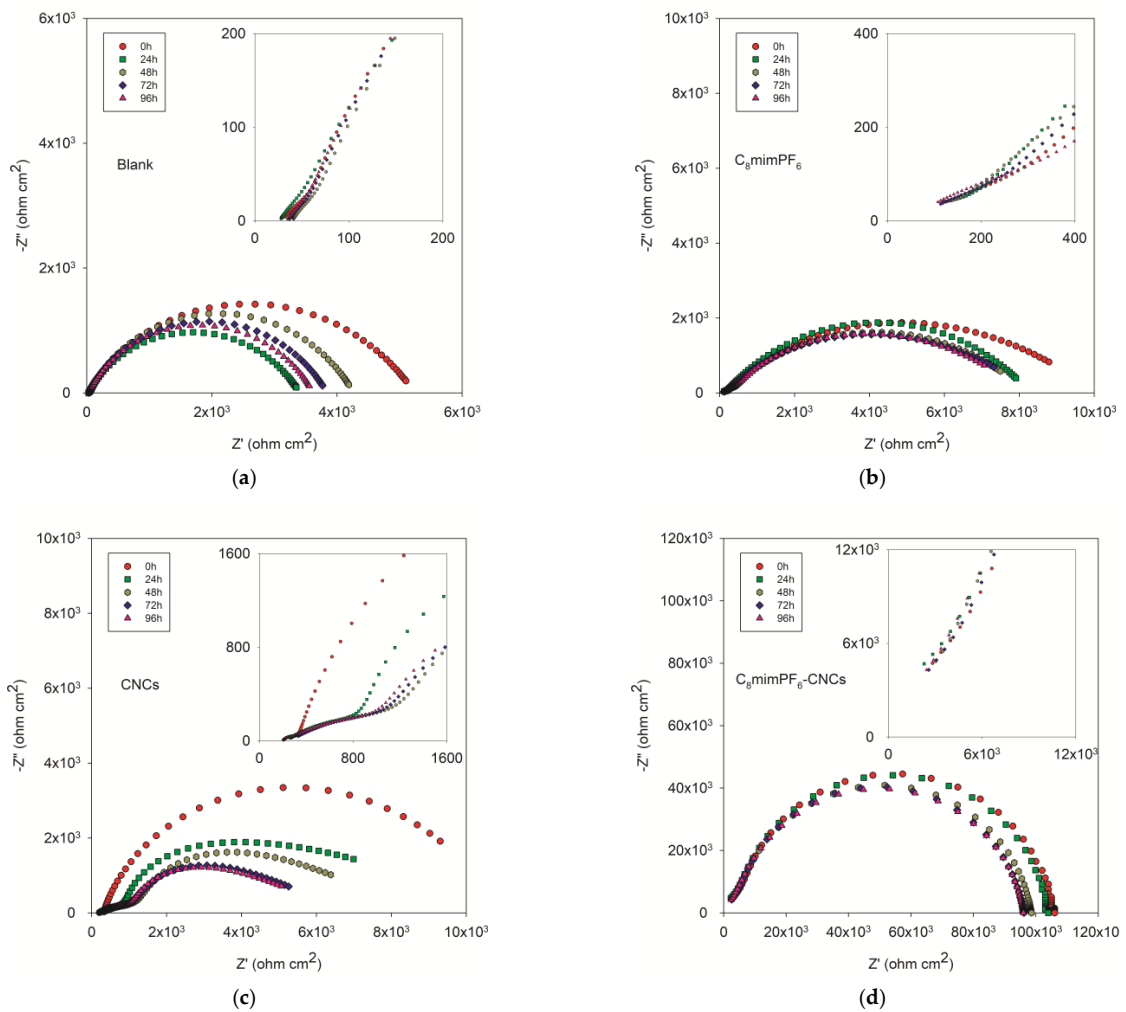


Figure 2. Nyquist impedance plots of coated samples after 96 h of immersion in 3.5 wt% NaCl solution. (a) Blank (neat PMMA-co-PBA coating), (b) $C_8\text{mimPF}_6$ (PMMA-co-PBA coating with 10 wt% $C_8\text{mimPF}_6$), (c) CNCs (PMMA-co-PBA coating with 0.5 wt% CNCs), and (d) $C_8\text{mimPF}_6$ -CNCs (PMMA-co-PBA coating with 10 wt% $C_8\text{mimPF}_6$ and 0.5 wt% CNCs).

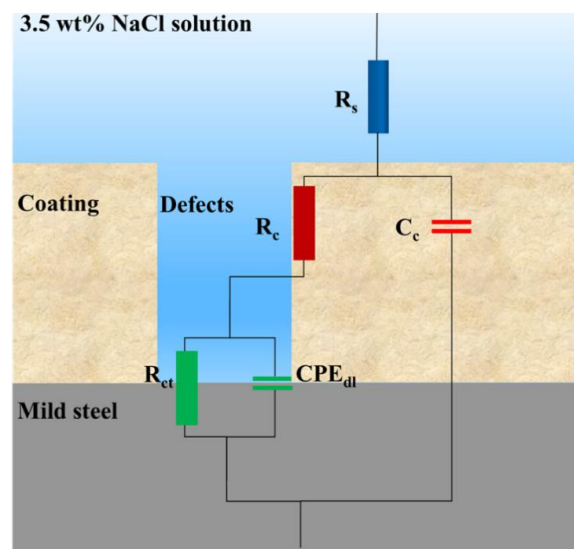


Figure 3. Equivalent circuit for EIS data fitting.

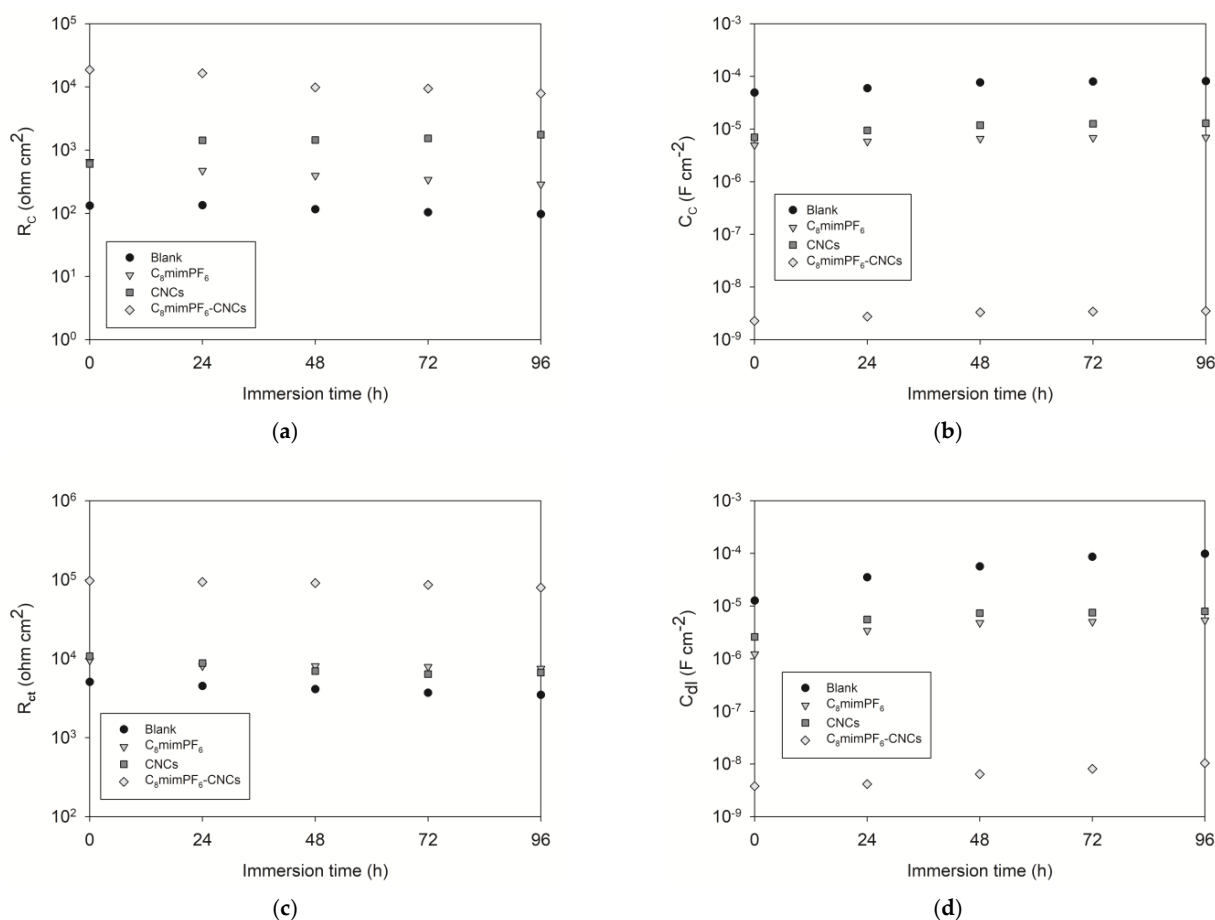


Figure 4. EIS parameters of coated samples in 3.5 wt% NaCl solution at different immersion periods. (a) Coating resistance, R_C , (b) coating capacitance, C_C , (c) charge transfer resistance, R_{ct} , and (d) double-layer capacitance, CPE_{dl} .

R_C indicates the barrier performance to ionic paths through the coating [24]. Generally, R_C values decreased with immersion time, which reveals a degradation of the coating and a decline in anti-corrosion performance [25]. As Figure 4 shows, the R_C value of the blank sample decreased from $132 \Omega \text{ cm}^2$ at the initial stage to $97 \Omega \text{ cm}^2$ after 96 h of immersion. Meanwhile, the R_C of the C₈mimPF₆ sample reduced from $624 \Omega \text{ cm}^2$ to $142 \Omega \text{ cm}^2$. The reduction in coating resistance shows the degradation of the coating. The final R_C for the C₈mimPF₆ sample was still higher than the blank sample, which indicates the prior anti-corrosion performance of the C₈mimPF₆ sample compared with the blank one. In contrast to the C₈mimPF₆ sample, the R_C of the CNCs sample increased significantly from $603 \Omega \text{ cm}^2$ at the initial stage to $1754 \Omega \text{ cm}^2$ after 96 h immersion. One explanation for this is the enhancement of the barrier effect after introducing CNCs into the coating [10]. Another possible reason may be a pseudo-two-time constant phenomenon after the penetration of electrolytes [21,22], which interferes with the curve fitting, resulting in a larger R_C value than the real value. During the immersion process, the R_C of the C₈mimPF₆-CNCs sample had the highest values of $18,670$ and $7865 \Omega \text{ cm}^2$ at the initial stage and after 96 h of immersion, respectively. This value was almost 100 times higher than the R_C of the blank sample, indicating the remarkable protective capability against corrosion with the combination of C₈mimPF₆ and CNCs. In addition, the charge transfer resistance, R_{ct} , the resistance to charge transfer on mild steel, was inversely related to the corrosion rate [26]. Similar to the results of R_C , the blank sample presented the lowest R_{ct} at $3490 \Omega \text{ cm}^2$ after 96 h of immersion. The R_{ct} s of the C₈mimPF₆ and CNCs samples were 7518 and $6677 \Omega \text{ cm}^2$, respectively, after 96 h of immersion, which was much higher than the R_{ct} of the blank sample, indicating an enhancement in charge transfer resistance with effect of adding these

two components. Surprisingly, the C_8mimPF_6 -CNCs sample exhibited the highest R_{ct} of $79,460 \Omega \text{ cm}^2$ after 96 h of immersion, which was nearly 22 times larger than the R_{ct} of the blank sample and one magnitude larger than that of the C_8mimPF_6 or CNCs samples. After immersion tests, Lewis et al. [27] studied the corrosion resistance of a $60 \mu\text{m}$ -thick waterborne acrylic coating modified with nano-sized titanium dioxide and found that the highest resistance after 48 h of immersion in 3% (m/v) NaCl solution was approximately $18,000 \Omega \text{ cm}^2$. Our C_8mimPF_6 -CNCs sample with a lower thickness and higher resistance is clearly more competitive, demonstrating that the lowest corrosion rate could be achieved under the synergistic effects of C_8mimPF_6 and CNCs.

In addition to resistance, the coating capacitance (C_C) and double-layer capacitance (CPE_{dl}) also indicate the extent of corrosion; the increase in capacitance indicates a rise in electrolyte uptake [25]. This study revealed the synergistic effect of C_8mimPF_6 and CNCs on capacitance, presented as the electrolyte uptake (water absorption) ratio and diffusion coefficient of corrosive ions. The main component of the electrolyte is water; therefore, the electrolyte uptake in this experiment is mainly water absorption. The Brasher and Kingsbury equation [18] was applied to calculate the volume fraction of water absorption, ϕ %:

$$\phi\% = \frac{\log\left(\frac{C_t}{C_0}\right)}{\log\epsilon_w} \times 100\% \quad (1)$$

where C_0 and C_t are the coating capacitance at the initial stage and time t , respectively. ϵ_w is the dielectric constant of the electrolyte (78.3 at 25°C for water [28]).

In Figure 5, the calculated absorbed water volume fraction at different immersion times is displayed. Waterborne acrylate coatings tend to absorb water due to the existence of a surfactant residue. After 96 h of immersion, the absorbed water volume fraction of the blank sample reached 11.4%. The CNCs sample presented the largest water absorption at 14.2%, which might be due to an enhancement in hydrophilicity caused by the hydrophilic functional groups, such as hydroxyl, carboxyl, and aldehyde groups, inside CNCs [29]. These hydrophilic functional groups favor water retention in the coating. In contrast, the C_8mimPF_6 sample exhibited the lowest absorbed water volume fraction of 7.7%, due to existence of a hydrophobic functional group, PF_6^- . As a result of this trade-off, the absorbed water volume fraction of the C_8mimPF_6 -CNCs sample was in between the value of the CNCs and C_8mimPF_6 samples.

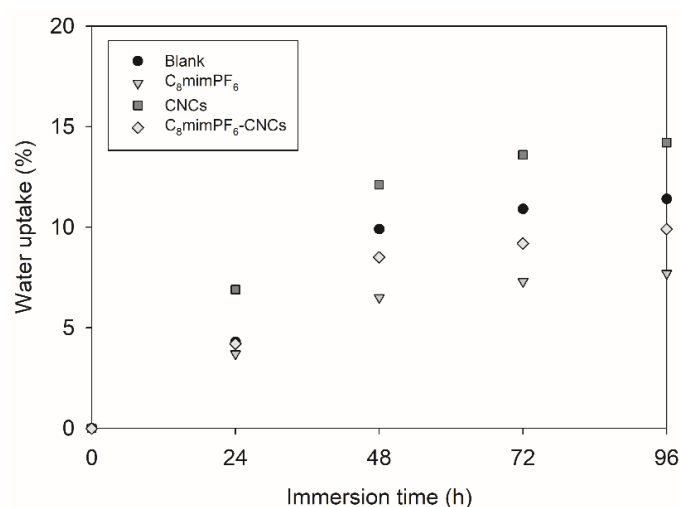


Figure 5. Water uptake of different coated samples immersed for up to 96 h.

The absorbed water volume fraction measures the moisture content retained in the coating. The concept of the electrolyte diffusion coefficient, D , is introduced to evaluate how fast the corrosive ions in the water moisture could pass through the coating. The diffusion coefficient, also called the diffusivity, indicates the ability of the corrosive ions to

penetrate through the coating. In this study, D was calculated using coating capacitance, CC , via a simplified Fick's law of diffusion [3]:

$$\frac{\lg C_c - \lg C_0}{\lg C_\infty - \lg C_0} = \frac{2}{L} \sqrt{\frac{D}{\pi}} \sqrt{t} \quad (2)$$

where C_0 , C_c , and C_∞ are the initial, current, and saturated coating capacitances. L is the coating thickness and D is the diffusion coefficient.

From Figure 6, after the introduction of $C_8\text{mimPF}_6$ and CNCs, the diffusion coefficient of each sample reduced from 3.6×10^{-11} to 1.1×10^{-12} and $7.7 \times 10^{-12} \text{ cm}^2 \cdot \text{s}^{-1}$, respectively. The $C_8\text{mimPF}_6$ -CNCs sample presented the lowest diffusion coefficient of $7.4 \times 10^{-14} \text{ cm}^2 \cdot \text{s}^{-1}$, where CNCs enhanced the barrier effect of the PMMA-co-PBA coating film and $C_8\text{mimPF}_6$ inhibited the corrosion of the mild steel surface [1,9,10]. In comparison, Ji et al. [30] used the same formula to calculate the diffusion coefficient of corrosive ions in a waterborne acrylic-alkyd anti-corrosion coating and reported that the lowest diffusion coefficient was $1.7 \times 10^{-11} \text{ cm}^2 \cdot \text{s}^{-1}$ at 25% alkyd, which is higher than the D of the $C_8\text{mimPF}_6$ and CNCs samples and much higher than the D of the $C_8\text{mimPF}_6$ -CNCs sample. This result further confirms the synergistic effect of $C_8\text{mimPF}_6$ and CNCs on anti-corrosion performance enhancement.

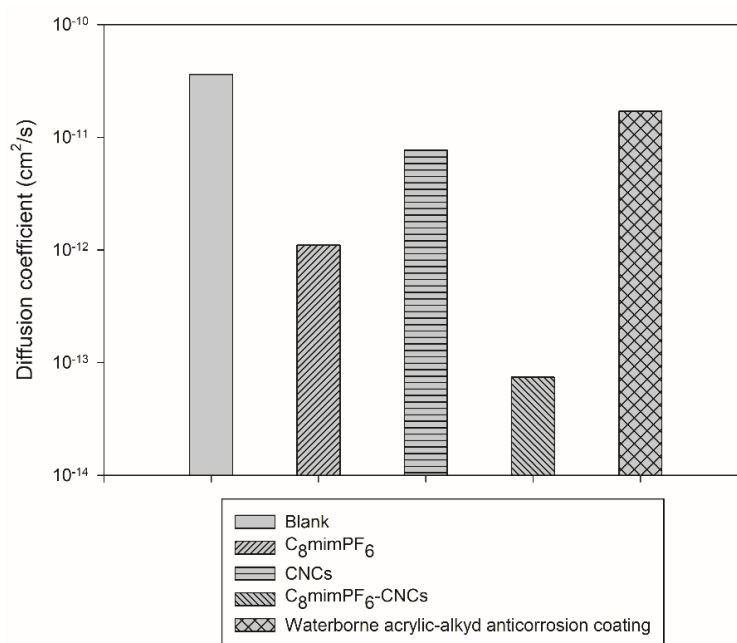


Figure 6. Diffusion coefficients of various coated samples.

3.1.3. Tafel Polarization Plot

In addition to EIS, Tafel polarization is another electrochemical technique to quantitatively evaluate the anti-corrosion performance based on the corrosion potential (E_{corr}) and the corrosion current density (i_{corr}). Additionally, i_{corr} is used to calculate two parameters of anti-corrosion performance: the corrosion inhibition efficiency and the corrosion rate. Figure 7 presents the Tafel plots of coated and uncoated samples after 96 h of immersion. The parameters and calculated variables of these Tafel plots are given in Table 1. Besides the corrosion potential (E_{corr}) and corrosion current density (i_{corr}), anodic and cathodic Tafel slopes b_a and b_c were also derived from the Tafel extrapolation of the plot in Figure 7. For bare mild steel, E_{corr} was -646 mV, and with the coating of neat PMMA-co-PBA, E_{corr} was -605 mV. After incorporating $C_8\text{mimPF}_6$ and CNCs, the E_{corr} for the $C_8\text{mimPF}_6$ and CNCs samples shifted to -534 and -550 mV, respectively. The least negative E_{corr} was obtained at -467 mV for the $C_8\text{mimPF}_6$ -CNCs sample. The less negative values of E_{corr} indicated

the enhancement in the anti-corrosion performance [31]. Therefore, E_{corr} results proved the optimal anticorrosion performance was in the C_8mimPF_6 -CNCs sample.

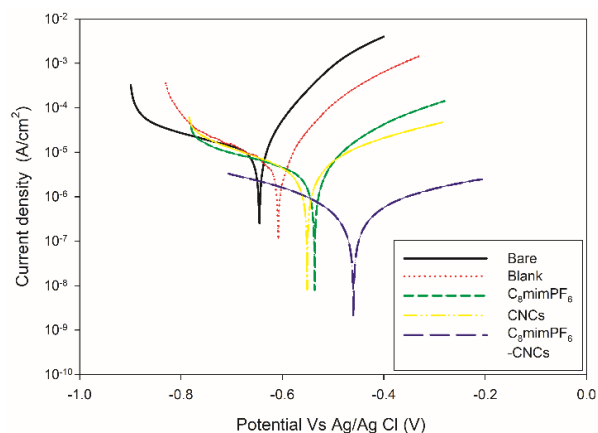


Figure 7. Tafel plots of coated and uncoated samples after 96 h of immersion.

Table 1. Tafel parameters and calculated corrosion variables of the coated and uncoated samples after 96 h of immersion.

| Sample | E_{corr} (mV) | I_{corr} ($\mu A/cm^2$) | b_a (V·dec ⁻¹) | b_c (V·dec ⁻¹) | Inhibition Efficiency | R_{corr} (μm per Year) |
|--------------------|-----------------|-----------------------------|------------------------------|------------------------------|-----------------------|--------------------------------|
| Bare steel | −646 | 9.4 | 61 | −334 | | 109 |
| Blank | −605 | 4.6 | 82 | −222 | 51% | 54 |
| C_8mimPF_6 | −534 | 2.9 | 103 | −305 | 70% | 34 |
| CNCs | −550 | 3.1 | 138 | −287 | 67% | 36 |
| C_8mimPF_6 -CNCs | −467 | 0.5 | 173 | −112 | 94% | 6 |

As for the corrosion current density (i_{corr}), instead of a direct comparison, it is used to calculate the corrosion inhibition efficiency ($IE\%$) and corrosion rate (V_{corr}) using Equations (3) and (4), respectively [3]:

$$IE\% = \frac{i_0 - i}{i_0} \times 100\% \tag{3}$$

where i_0 and i are corrosion current densities of uncoated and coated samples, respectively, after 96 h of immersion at room temperature.

The $IE\%$ s were 51% (blank), 70% (C_8mimPF_6), 67% (CNCs), and 94% (C_8mimPF_6 -CNCs) which proved the improvement in anti-corrosion performance under the synergistic effect of C_8mimPF_6 and CNCs. Hamidon and Hussin [32] studied the synergistic anti-corrosion impact of a hybrid silane/silicate sol-gel and caffeine in a 3.5 wt% NaCl solution. They stated that the highest inhibition efficiency was 89% at 100 ppM caffeine. Compared with this, our product was better at inhibiting the corrosion of mild steel in 3.5 wt% NaCl. Therefore, the combination of C_8mimPF_6 and CNCs would be a competitive method to use in the anti-corrosion of mild steel in 3.5 wt% NaCl solutions. In addition, our C_8mimPF_6 -CNCs sample was advantageous for the same corrosion inhibition during the immersion period. Murmu et al. [33] used p-phenylenediamine to cure double Schiff base epoxy (DSBE) and applied it to coating of mild steel in a 3.5 wt% NaCl solution. The highest inhibition efficiency was 94% after 24 h of immersion, similar to the $IE\%$ of our products after 96 h of immersion.

The corrosion rate (V_{corr} , mm per year) was also calculated from i_{corr} using Equation (4), and the results are shown in Table 1 [34].

$$V_{corr} = \frac{i_{corr}M}{DV} \times 3270 \quad (4)$$

where i_{corr} is the corrosion current density (A/cm^2), M is molecular weight (56 g mol^{-1} for mild steel), V is the valency (two for the oxidation of mild steel), 3270 ($\text{mm} \cdot \text{g} \cdot \text{A}^{-1} \cdot \text{cm}^{-1} \cdot \text{year}^{-1}$) is a constant for unit conversion [35], and D is the density (7.85 g cm^{-3} for mild steel).

The corrosion rate of these samples was consistent with the results of corrosion inhibition efficiency. The results showed that V_{corr} decreased from $109 \mu\text{m}$ per year (bare) to $54 \mu\text{m}$ per year (blank). With the addition of C_8mimPF_6 and CNCs, it further decreased to 34 (C_8mimPF_6) and 36 (CNCs) μm per year. The synergistic effect of C_8mimPF_6 -CNCs was further proven with the lowest V_{corr} of $6 \mu\text{m}$ per year, which was $1/18$ of the V_{corr} of the blank sample. In comparison, Cai et al. [36] introduced polyaniline (PANI) and reduced graphene oxide (RGO) as anti-corrosive fillers into a waterborne polyurethane coating and found that the lowest V_{corr} was achieved at 0.75 wt\% RGO/PANI, which was about $1/6$ of that of the neat waterborne polyurethane (blank sample).

3.1.4. Morphology after Immersion Tests

The optimal anti-corrosion performance of the C_8mimPF_6 -CNCs was further investigated using SEM. The surface morphology with a 500 times magnification for samples before and after immersion was observed and is displayed in Figure 8. Before the immersion test, all coated samples presented a smooth surface with a few residues of copolymer particles on the surface. After the immersion test, rust covered the surface of bare mild steel, which indicated its poor anti-corrosion performance. With the coating of neat PMMA-co-PBA, the surface exhibited some defects instead of the rust observed in the blank sample, which was a sign of anti-corrosion enhancement. After incorporating C_8mimPF_6 or CNCs, defects were replaced with a small number of cracks, indicating a further improvement in anti-corrosion properties. With the synergistic effect of C_8mimPF_6 and CNCs, the C_8mimPF_6 -CNCs sample exhibited optimal anti-corrosion performance with sparse cracks and a smooth surface.

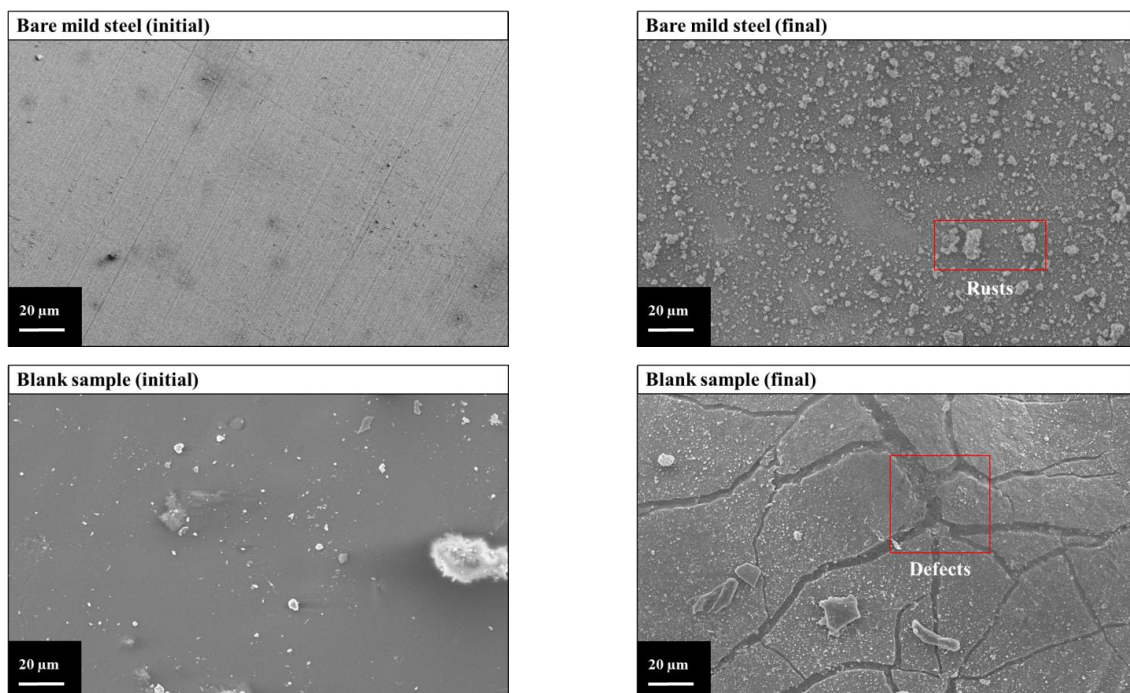


Figure 8. Cont.

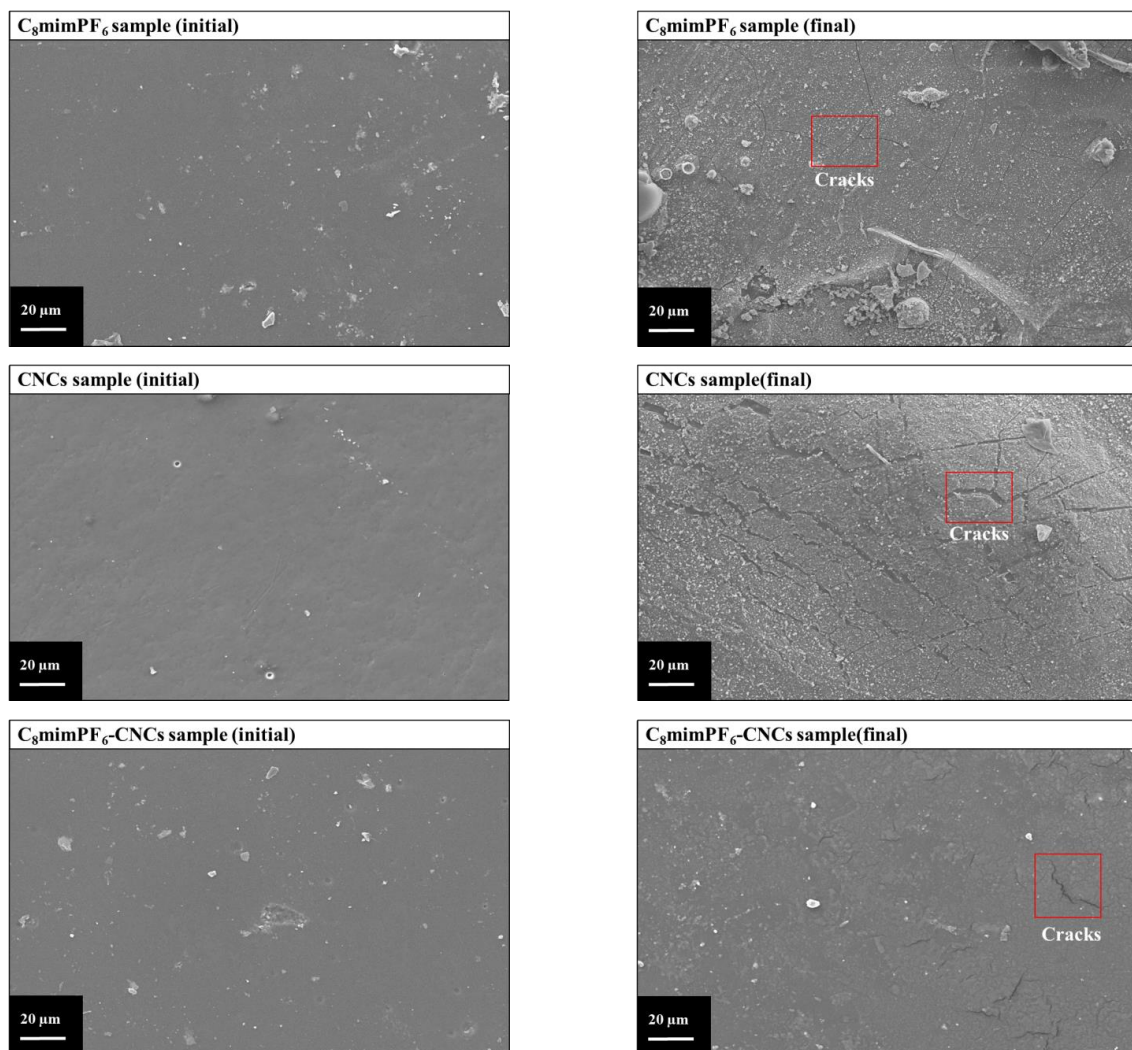


Figure 8. Surface morphology of coated and uncoated samples before and after 96 h of immersion in 3.5 wt% NaCl solution (500 times magnification).

3.2. Mechanism of C_8mimPF_6 and CNCs in PMMA-co-PBA Anti-Corrosion Coating

The results above have proved the synergistic anti-corrosion effects of C_8mimPF_6 and CNCs in PMMA-co-PBA coatings. To further explain the mechanism of this synergistic effect, the status of the C_8mimPF_6 and CNCs in the coating and the wettability of the coating were observed, and a possible detailed mechanism was illustrated with a schematic drawing.

3.2.1. Status Identification of C_8mimPF_6 and CNCs in PMMA-co-PBA Coating

To identify the status of C_8mimPF_6 and CNCs in the PMMA-co-PBA coating, the FTIR spectra of the as-received C_8mimPF_6 and CNCs and the as-prepared samples were measured and plotted in Figure 9. For C_8mimPF_6 , characteristic peaks of C_8mim^+ were present at 3173 cm^{-1} (aromatic n(C-H) stretching vibration), 1574 cm^{-1} (imidazolium H-C-C bending), 1469 cm^{-1} (imidazolium H-C-N bending), and 1168 cm^{-1} (imidazolium C2-N1-C5 bending), and the peaks at 837 (P-F stretching vibration) and 558 cm^{-1} (P-F bending vibration) were assigned to PF_6^- [37–39]. Meanwhile, the distinct characteristic peaks of CNCs were 1161 cm^{-1} (C-O-C vibration in pyranose ring), 1060 cm^{-1} (C-O-C asymmetric stretching vibration), and 896 cm^{-1} (β -glycosidic linkages of glucose ring) [40–43]. For neat PMMA-co-PBA, peaks at 2997 , 2952 , and 1444 cm^{-1} represented the $-CH_3$ stretching vibration, the $-CH_2-$ stretching vibration, and the C-H bending vibration, respectively [44].

In addition, the carboxyl group's C–O–C stretching vibration induced peaks at 1732, 1250, and 1150 cm^{-1} [44,45]. In the C_8mimPF_6 copolymer sample, peaks at 837 cm^{-1} and 558 cm^{-1} were observed, which proved the existence of C_8mimPF_6 . Moreover, the peak at 1060 cm^{-1} demonstrated the existence of cellulose C–O–C functional groups in the CNCs copolymer sample; the peak might be overlapped by the peak of the carboxyl stretching vibration in the copolymer at 1150 cm^{-1} . In the C_8mimPF_6 -CNCs copolymer sample, these peaks mentioned above were all observed, and confirmed the co-existence of C_8mimPF_6 and CNCs. As for the interaction between C_8mimPF_6 and CNCs, it has been reported that cellulose can be dissolved in some kinds of ionic liquids [46]. However, the solubility of lignocellulose in imidazolium ionic liquid with PF_6^- anions was extremely low (0.1%) [47]. Therefore, CNCs were not dissolved in C_8mimPF_6 . Moreover, C_8mimPF_6 and CNCs do not contain vinyl or styrene groups. No other new peaks aside from the C_8mimPF_6 and CNCs peaks were observed in the spectrum. Thus, it can be concluded that C_8mimPF_6 and CNCs did not attend the reaction. Due to the stabilizing properties of CNCs reported in the previous literature [48], CNCs might form strong physical interactions with PMMA-co-PBA. It is speculated that C_8mimPF_6 was encapsulated in a PMMA-co-PBA droplet, and CNCs behaved as a co-stabilizer adsorbed on the droplet surface.

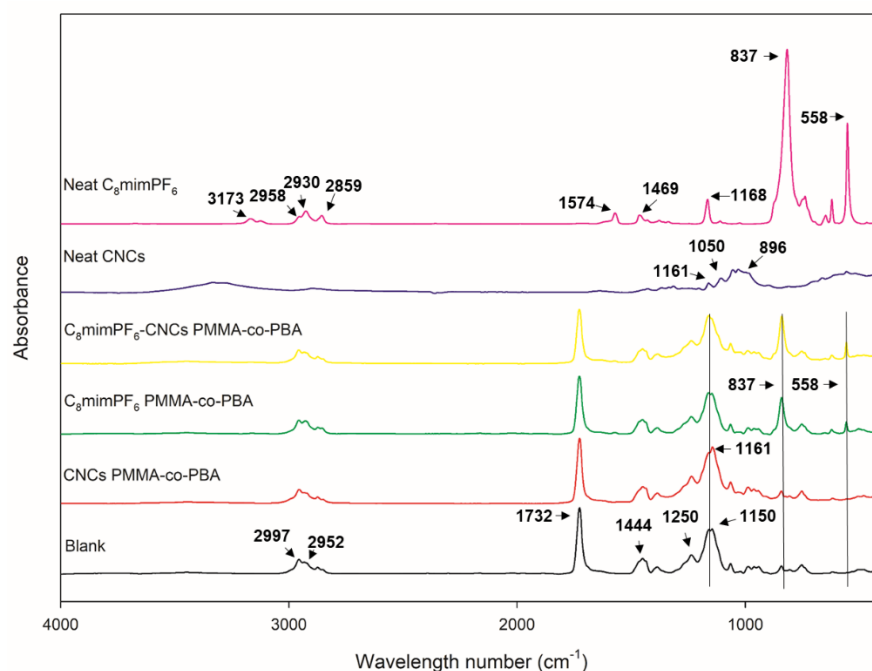


Figure 9. FTIR spectra for various samples.

3.2.2. Wettability of Copolymer Coating

The wettability of the copolymer coating is another concern, because the hydrophobicity of the coating may influence the anti-corrosion performance [49]. Surface roughness and surface chemistry are the two main factors affecting the wettability [50,51]. Based on the results of SEM, the surface morphology of each sample was similar, so the influence of surface roughness on the contact angle was negligible. Therefore, the variation in contact angle obtained for each sample could be ascribed to the surface chemistry. As shown in Figure 10, the water contact angle of the blank sample (neat PMMA-co-PBA) was approximately 79.8°. Due to the typical hydrophobic anion PF_6^- , the introduction of C_8mimPF_6 improved the hydrophobicity up to a water contact angle of 83.5°. In contrast, the hydrophobicity of the copolymer coating weakened, and the water contact angle decreased to 76.6° after adding CNCs, influenced by the abundance of hydrophilic functional groups such as hydroxyl, carboxyl, and aldehyde groups [26]. As for the C_8mimPF_6 -CNCs sample, the water contact angle was about 81.4°, located between the values of C_8mimPF_6 and CNCs samples. These

were consistent with the results of water absorption in Section 3.2.2. The incorporation of C_8mimPF_6 and CNCs influenced the wettability of the coating and further affected the water absorption.

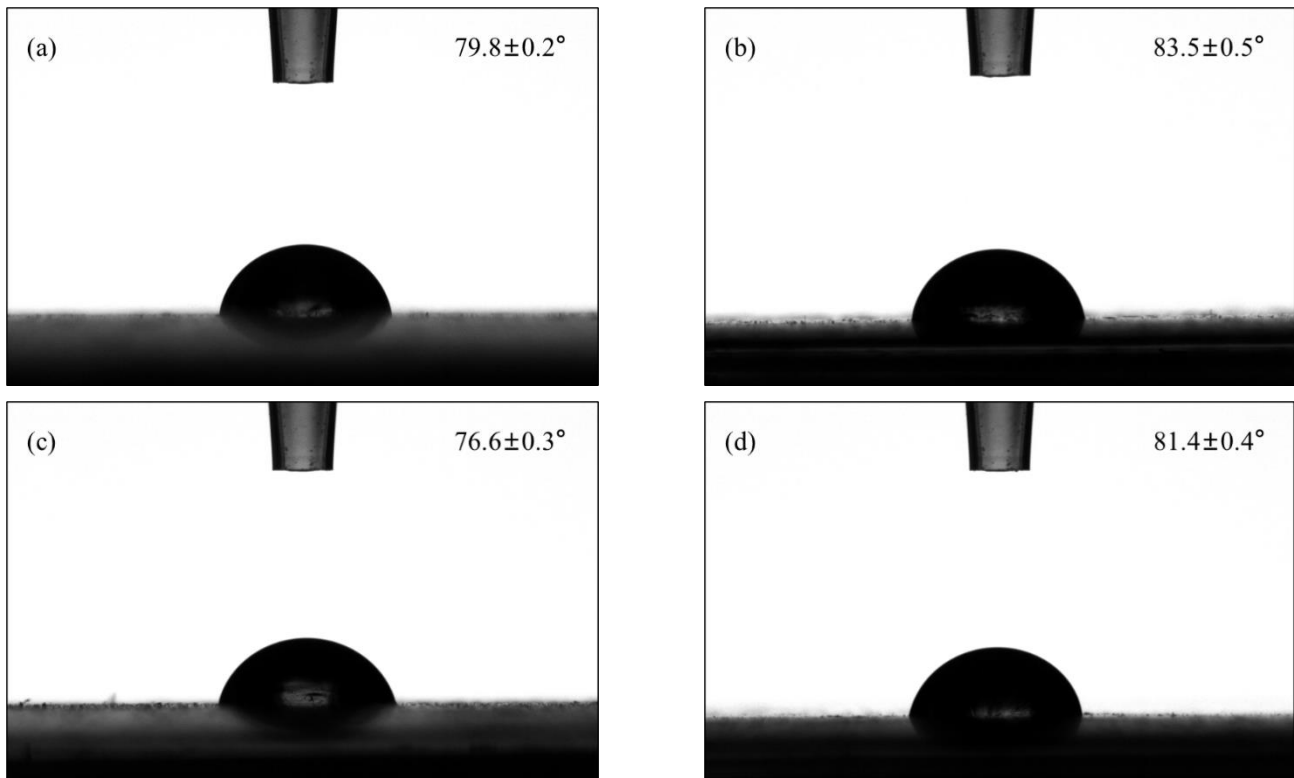


Figure 10. The water contact angle for various coated samples (a) blank sample, (b) C_8mimPF_6 , (c) CNCs, (d) C_8mimPF_6 -CNCs.

3.2.3. Synergistic Effect of C_8mimPF_6 and CNCs in PMMA-co-PBA Anti-Corrosion Coatings

With all the results listed above, the synergistic anti-corrosion mechanism of C_8mimPF_6 and CNCs could be summarized. As shown in Figure 11, at the initial stage of immersion, oxygen, moisture, and other corrosive ions such as Cl^- diffuse through the micropores and defects of the copolymer coating to the coating interface and mild steel. Without C_8mimPF_6 and CNCs, oxidation and reduction occurred at the interface listed below [52].



Pitting and delamination of coatings could be induced by these reactions, followed by failure of the protective effect. With the introduction of CNCs, a barrier effect enhancement was observed with a higher coating resistance and lower diffusion coefficient, which might be caused by the reinforcing and impermeable properties of CNCs [9,10]. However, the reduction in the water contact angle and larger water absorption volume ratio compared to the blank sample indicates that there was more water moisture absorbed in the coating. Despite the fact that more water moisture was absorbed, the anti-corrosion performance was still enhanced in the CNCs sample. In other words, most of the water moisture in the CNCs sample was contained to the coating without further penetration through the coating layer. This is similar to other nanofillers, such as nano silica, which can retard the

diffusion of water moisture and other corrosive ions to the coating/mild steel interface through zigzagging the pathway [53,54]. Nevertheless, even though the barrier effect of the coating was enhanced, some of the water moisture and other corrosive ions could still pass through the coating and be retained at the interface of coating and mild steel, which could still induce corrosion. With further degradation of the coating film, encapsulated C_8mimPF_6 was released and C_8mim^+ cations replaced Na^+ , adsorbing electrostatically on the surface of the mild steel due to its larger steric hindrance [1,2,55–57]. Then, the corrosion rate was further reduced as the corrosion reaction sites on the mild steel were blocked. In summary, CNCs and C_8mimPF_6 worked at different coating sites, where CNCs strengthened the barrier effect of the coating and C_8mimPF_6 inhibited the corrosion at the interface of the coating and the mild steel. Therefore, the C_8mimPF_6 -CNCs composite coating exhibited superior protection than other samples in this research with the highest corrosion inhibition efficiency, the lowest diffusion coefficient and corrosion rate, and the least corroded surface, as observed by SEM.

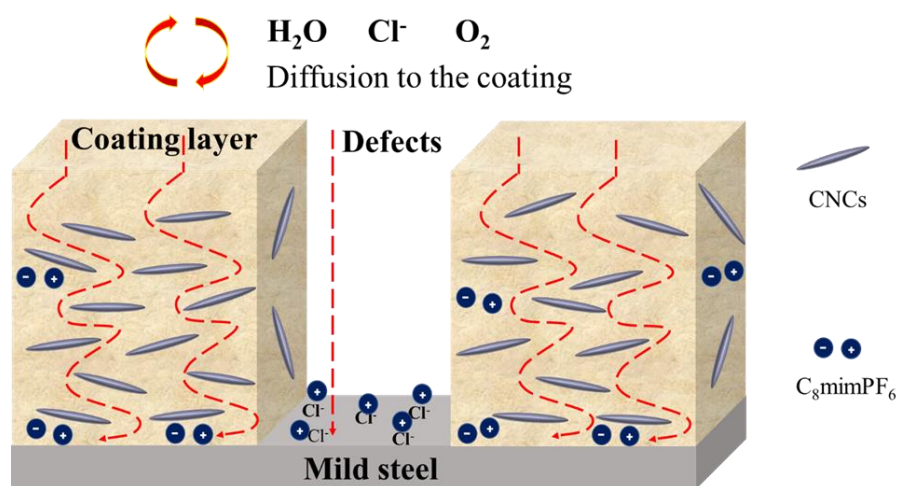


Figure 11. Schematic representation of corrosion protection for mild steel with the C_8mimPF_6 -CNCs sample.

As for the interaction between $CmimPF_6$ and CNCs, no new peaks were observed in FTIR results. Although it has been reported that either a catalyst or a linker is required at a higher temperature such as $170\text{ }^\circ\text{C}$ to graft imidazolium ions onto CNCs [13,58]. Therefore, it could be concluded that no chemical interaction existed between C_8mimPF_6 and CNCs in our products.

4. Conclusions

A waterborne PMMA-co-PBA latex incorporated with C_8mimPF_6 and CNCs was successfully prepared through mini emulsion polymerization. FTIR proved the incorporation of C_8mimPF_6 and CNCs, and the anti-corrosion performances of the copolymer coatings were investigated on mild steel samples exposed to 3.5 wt% NaCl. The C_8mimPF_6 -CNCs sample exhibited a superior anti-corrosion performance with the highest coating, charge transfer resistance, and corrosion inhibition efficiency and lowest diffusion coefficient. The proposed synergistic mechanism showed that the CNCs enhanced the barrier effect of the coating while the C_8mimPF_6 inhibited corrosion when released. This study reveals a way to combine two environmentally friendly additives with different anti-corrosive mechanisms to achieve a synergistic effect for anti-corrosion.

Author Contributions: Methodology, Z.W.; Validation, Z.W.; Formal analysis, Z.W.; Investigation, Z.W.; Resources, Z.W.; Data curation, Z.W.; Writing—original draft, Z.W.; Writing—review & editing, B.H., H.Y. and G.Z.C.; Project administration, B.H.; Funding acquisition, B.H. All authors have read and agreed to the published version of the manuscript.

Funding: This research and APC was funded by Zhejiang Yuxi Corrosion Control Corporation, grant number (01.03.07.01.2015.06.002). Ph.D. scholarship is funded by the University of Nottingham Ningbo China and Provincial Key Lab Pro-gram, grant number (2020E10018); Part of the sample analysis and Prof Haibin Yu's work are funded by Science and Technology Innovation 2025" Major Projects, Grant/Award Numbers:2020Z087, 2019B10062.

Institutional Review Board Statement: Not applicable.

Informed Consent Statement: Not applicable.

Data Availability Statement: The data presented in this study are available on request from the corresponding author.

Conflicts of Interest: The authors declare no conflict of interest.

References

1. Wang, Z.; Hu, B.; Chen, G.Z. The role of 1-octyl-3-methylimidazolium hexafluorophosphate in anticorrosion coating formula development. *J. Saudi Chem. Soc.* **2022**, *26*, 101446. [[CrossRef](#)]
2. Likhanova, N.V.; Domínguez-Aguilar, M.A.; Olivares-Xometl, O.; Nava-Entzana, N.; Arce, E.; Dorantes, H. The effect of ionic liquids with imidazolium and pyridinium cations on the corrosion inhibition of mild steel in acidic environment. *Corros. Sci.* **2010**, *52*, 2088–2097. [[CrossRef](#)]
3. Ding, J.; Shi, S.; Yu, H. Study on modification of lignin as dispersant of aqueous graphene suspension and corrosion performance in waterborne G/epoxy coating. *Int. J. Adv. Eng. Res. Sci.* **2016**, *3*, 101–112. [[CrossRef](#)]
4. Carretti, E.; Dei, L. Physicochemical characterization of acrylic polymeric resins coating porous materials of artistic interest. *Prog. Org. Coat.* **2004**, *49*, 282–289. [[CrossRef](#)]
5. Du, B.; Chen, F.; Luo, R.; Zhou, S.; Wu, Z. Synthesis and characterization of nano-TiO₂/SiO₂-acrylic composite resin. *Adv. Mater. Sci. Eng.* **2019**, *2019*, 6318623. [[CrossRef](#)]
6. Zhan, Y.; Meng, Y.; Li, Y.; Zhang, C.; Xie, Q.; Wei, S.; Lavorgna, M.; Chen, Z. Poly (vinyl alcohol)/reduced graphene oxide multilayered coatings: The effect of filler content on gas barrier and surface resistivity properties. *Compos. Commun.* **2021**, *24*, 100670. [[CrossRef](#)]
7. George, J.; Sabapathi, S. Cellulose nanocrystals: Synthesis, functional properties, and applications. *Nanotechnol. Sci. Appl.* **2015**, *8*, 45. [[CrossRef](#)]
8. Xu, X.; Liu, F.; Jiang, L.; Zhu, J.; Haagenson, D.; Wiesenborn, D.P. Cellulose nanocrystals vs. cellulose nanofibrils: A comparative study on their microstructures and effects as polymer reinforcing agents. *ACS Appl. Mater. Interfaces* **2013**, *5*, 2999–3009. [[CrossRef](#)]
9. Fukuzumi, H.; Saito, T.; Iwata, T.; Kumamoto, Y.; Isogai, A. Transparent and high gas barrier films of cellulose nanofibers prepared by TEMPO-mediated oxidation. *Biomacromolecules* **2008**, *10*, 162–165. [[CrossRef](#)]
10. Follain, N.; Belbekhouche, S.; Bras, J.; Siqueira, G.; Marais, S.; Dufresne, A. Water transport properties of bio-nanocomposites reinforced by *Luffa cylindrica* cellulose nanocrystals. *J. Membr. Sci.* **2013**, *427*, 218–229. [[CrossRef](#)]
11. He, Y.; Boluk, Y.; Pan, J.; Ahniyaz, A.; Deltin, T.; Claesson, P.M. Corrosion protective properties of cellulose nanocrystals reinforced waterborne acrylate-based composite coating. *Corros. Sci.* **2019**, *155*, 186–194. [[CrossRef](#)]
12. Liu, P.; Guo, X.; Nan, F.; Duan, Y.; Zhang, J. Modifying mechanical, optical properties and thermal processability of iridescent cellulose nanocrystal films using ionic liquid. *ACS Appl. Mater. Interfaces* **2017**, *9*, 3085–3092. [[CrossRef](#)] [[PubMed](#)]
13. Wang, L.; Hu, J.; Liu, Y.; Shu, J.; Wu, H.; Wang, Z.; Pan, X.; Zhang, N.; Zhou, L.; Zhang, J. Ionic liquids grafted cellulose nanocrystals for high-strength and toughness PVA nanocomposite. *ACS Appl. Mater. Interfaces* **2020**, *12*, 38796–38804. [[CrossRef](#)]
14. Wahib, S.A.; Da'na, D.A.; Zaouri, N.; Hijji, Y.M.; Al-Ghouti, M.A. Adsorption and recovery of lithium ions from groundwater using date pits impregnated with cellulose nanocrystals and ionic liquid. *J. Hazard. Mater.* **2022**, *421*, 126657. [[CrossRef](#)] [[PubMed](#)]
15. Tait, W.S. Electrochemical corrosion basics. In *Handbook of Environmental Degradation of Materials*; Elsevier: Amsterdam, The Netherlands, 2018; pp. 97–115.
16. Ghasemi-Kahrizsangi, A.; Shariatpanahi, H.; Neshati, J.; Akbarinezhad, E. Corrosion behavior of modified nano carbon black/epoxy coating in accelerated conditions. *Appl. Surf. Sci.* **2015**, *331*, 115–126. [[CrossRef](#)]
17. Qiu, S.; Li, W.; Zheng, W.; Zhao, H.; Wang, L. Synergistic effect of polypyrrole-intercalated graphene for enhanced corrosion protection of aqueous coating in 3.5% NaCl solution. *ACS Appl. Mater. Interfaces* **2017**, *9*, 34294–34304. [[CrossRef](#)] [[PubMed](#)]
18. Brasher, D.; Kingsbury, A. Electrical measurements in the study of immersed paint coatings on metal. I. Comparison between capacitance and gravimetric methods of estimating water-uptake. *J. Appl. Chem.* **1954**, *4*, 62–72. [[CrossRef](#)]
19. Orazem, M.E.; Tribollet, B. *Electrochemical Impedance Spectroscopy*; John Wiley & Sons: Hoboken, NJ, USA, 2011.
20. Orazem, M.E.; Pébère, N.; Tribollet, B. Enhanced graphical representation of electrochemical impedance data. *J. Electrochem. Soc.* **2006**, *153*, B129. [[CrossRef](#)]
21. Bagal, N.S.; Kathavate, V.S.; Deshpande, P.P. Nano-TiO₂ Phosphate Conversion Coatings—A Chemical Approach. *Electrochem. Energy Technol.* **2018**, *4*, 47–54. [[CrossRef](#)]

22. Kathavate, V.S.; Pawar, D.; Bagal, N.; Deshpande, P. Role of nano ZnO particles in the electrodeposition and growth mechanism of phosphate coatings for enhancing the anti-corrosive performance of low carbon steel in 3.5% NaCl aqueous solution. *J. Alloys Compd.* **2020**, *823*, 153812. [[CrossRef](#)]
23. Holm, S.; Holm, T.; Martinsen, Ø.G. Simple circuit equivalents for the constant phase element. *PLoS ONE* **2021**, *16*, e0248786. [[CrossRef](#)]
24. Cano, E.; Lafuente, D.; Bastidas, D.M. Use of EIS for the evaluation of the protective properties of coatings for metallic cultural heritage: A review. *J. Solid State Electrochem.* **2010**, *14*, 381–391. [[CrossRef](#)]
25. Mostafaei, A.; Nasirpour, F. Epoxy/polyaniline–ZnO nanorods hybrid nanocomposite coatings: Synthesis, characterization and corrosion protection performance of conducting paints. *Prog. Org. Coat.* **2014**, *77*, 146–159. [[CrossRef](#)]
26. Lu, H.; Zhang, S.; Li, W.; Cui, Y.; Yang, T. Synthesis of graphene oxide-based sulfonated oligoanilines coatings for synergistically enhanced corrosion protection in 3.5% NaCl solution. *ACS Appl. Mater. Interfaces* **2017**, *9*, 4034–4043. [[CrossRef](#)]
27. Lewis, O.; Critchlow, G.; Wilcox, G.; de Zeeuw, A.; Sander, J. A study of the corrosion resistance of a waterborne acrylic coating modified with nano-sized titanium dioxide. *Prog. Org. Coat.* **2012**, *73*, 88–94. [[CrossRef](#)]
28. Malmberg, C.; Maryott, A. Dielectric Constant of Water from 00 to 1000 C. *J. Res. Natl. Bur. Stand.* **1956**, *56*, 1. [[CrossRef](#)]
29. Fu, L.-H.; Qi, C.; Ma, M.-G.; Wan, P. Multifunctional cellulose-based hydrogels for biomedical applications. *J. Mater. Chem. B* **2019**, *7*, 1541–1562. [[CrossRef](#)] [[PubMed](#)]
30. Ji, S.; Gui, H.; Guan, G.; Zhou, M.; Guo, Q.; Tan, M.Y. Molecular design and copolymerization to enhance the anti-corrosion performance of waterborne acrylic coatings. *Prog. Org. Coat.* **2021**, *153*, 106140. [[CrossRef](#)]
31. Frankel, G. Fundamentals of corrosion kinetics. In *Active Protective Coatings*; Springer: Berlin/Heidelberg, Germany, 2016; pp. 17–32.
32. Hamidon, T.S.; Hussin, M.H. Susceptibility of hybrid sol-gel (TEOS-APTES) doped with caffeine as potent corrosion protective coatings for mild steel in 3.5 wt.% NaCl. *Prog. Org. Coat.* **2020**, *140*, 105478. [[CrossRef](#)]
33. Murmu, M.; Saha, S.K.; Murmu, N.C.; Banerjee, P. Amine cured double Schiff base epoxy as efficient anticorrosive coating materials for protection of mild steel in 3.5% NaCl medium. *J. Mol. Liq.* **2019**, *278*, 521–535. [[CrossRef](#)]
34. Weng, C.J.; Huang, J.Y.; Huang, K.Y.; Jhuo, Y.S.; Tsai, M.H.; Yeh, J.M. Advanced anticorrosive coatings prepared from electroactive polyimide–TiO hybrid nanocomposite materials. *Electrochim. Acta* **2010**, *55*, 8430–8438. [[CrossRef](#)]
35. Yeh, J.M.; Huang, H.Y.; Chen, C.L.; Su, W.F.; Yu, Y.H. Siloxane-modified epoxy resin–clay nanocomposite coatings with advanced anticorrosive properties prepared by a solution dispersion approach. *Surf. Coat. Technol.* **2006**, *200*, 2753–2763. [[CrossRef](#)]
36. Cai, K.; Zuo, S.; Luo, S.; Yao, C.; Liu, W.; Ma, J.; Mao, H.; Li, Z. Preparation of polyaniline/graphene composites with excellent anti-corrosion properties and their application in waterborne polyurethane anticorrosive coatings. *RSC Adv.* **2016**, *6*, 95965–95972. [[CrossRef](#)]
37. Iimori, T.; Iwahashi, T.; Kanai, K.; Seki, K.; Sung, J.; Kim, D.; Hamaguchi, H.-o.; Ouchi, Y. Local Structure at the Air/Liquid Interface of Room-Temperature Ionic Liquids Probed by Infrared–Visible Sum Frequency Generation Vibrational Spectroscopy: 1-Alkyl-3-methylimidazolium Tetrafluoroborates. *J. Phys. Chem. B* **2007**, *111*, 4860–4866. [[CrossRef](#)] [[PubMed](#)]
38. Aroca, R.; Nazri, M.; Nazri, G.; Camargo, A.; Trsic, M. Vibrational spectra and ion-pair properties of lithium hexafluorophosphate in ethylene carbonate based mixed-solvent systems for lithium batteries. *J. Solut. Chem.* **2000**, *29*, 1047–1060. [[CrossRef](#)]
39. Peng, B.; Zhang, J.; Lu, R.; Zhang, S.; Zhou, W.; Gao, H. Dispersive micro-solid phase extraction based on self-assembling, ionic liquid-coated magnetic particles for the determination of clofentazine and chlorfenapyr in environmental water samples. *Analyst* **2013**, *138*, 6834–6843. [[CrossRef](#)]
40. Mandal, A.; Chakraborty, D. Isolation of nanocellulose from waste sugarcane bagasse (SCB) and its characterization. *Carbohydr. Polym.* **2011**, *86*, 1291–1299. [[CrossRef](#)]
41. Wulandari, W.; Rochliadi, A.; Arcana, I. Nanocellulose prepared by acid hydrolysis of isolated cellulose from sugarcane bagasse. In *IOP Conference Series: Materials Science and Engineering*; IOP Publishing: Bristol, UK, 2016; Volume 107, p. 012045.
42. Alemdar, A.; Sain, M. Isolation and characterization of nanofibers from agricultural residues–Wheat straw and soy hulls. *Bioresour. Technol.* **2008**, *99*, 1664–1671. [[CrossRef](#)]
43. Lamaming, J.; Hashim, R.; Sulaiman, O.; Leh, C.P.; Sugimoto, T.; Nordin, N.A. Cellulose nanocrystals isolated from oil palm trunk. *Carbohydr. Polym.* **2015**, *127*, 202–208. [[CrossRef](#)]
44. Duan, G.; Zhang, C.; Li, A.; Yang, X.; Lu, L.; Wang, X. Preparation and characterization of mesoporous zirconia made by using a poly (methyl methacrylate) template. *Nanoscale Res. Lett.* **2008**, *3*, 118. [[CrossRef](#)]
45. Ramesh, S.; Leen, K.H.; Kumutha, K.; Arof, A. FTIR studies of PVC/PMMA blend based polymer electrolytes. *Spectrochim. Acta Part A Mol. Biomol. Spectrosc.* **2007**, *66*, 1237–1242. [[CrossRef](#)] [[PubMed](#)]
46. Pinkert, A.; Marsh, K.N.; Pang, S.; Staiger, M.P. Ionic liquids and their interaction with cellulose. *Chem. Rev.* **2009**, *109*, 6712–6728. [[CrossRef](#)] [[PubMed](#)]
47. Lee, S.H.; Doherty, T.V.; Linhardt, R.J.; Dordick, J.S. Ionic liquid-mediated selective extraction of lignin from wood leading to enhanced enzymatic cellulose hydrolysis. *Biotechnol. Bioeng.* **2009**, *102*, 1368–1376. [[CrossRef](#)] [[PubMed](#)]
48. Kalashnikova, I.; Bizot, H.; Cathala, B.; Capron, I. New Pickering emulsions stabilized by bacterial cellulose nanocrystals. *Langmuir* **2011**, *27*, 7471–7479. [[CrossRef](#)]

49. Ammar, S.; Ramesh, K.; Vengadaesvaran, B.; Ramesh, S.; Arof, A.K. Formulation and characterization of hybrid polymeric/ZnO nanocomposite coatings with remarkable anti-corrosion and hydrophobic characteristics. *J. Coat. Technol. Res.* **2016**, *13*, 921–930. [[CrossRef](#)]
50. Nakae, H.; Inui, R.; Hirata, Y.; Saito, H. Effects of surface roughness on wettability. *Acta Mater.* **1998**, *46*, 2313–2318. [[CrossRef](#)]
51. Mantel, M.; Wightman, J. Influence of the surface chemistry on the wettability of stainless steel. *Surf. Interface Anal.* **1994**, *21*, 595–605. [[CrossRef](#)]
52. Pech-Canul, M.; Bartolo-Perez, P. Inhibition effects of N-phosphono-methyl-glycine/Zn²⁺ mixtures on corrosion of steel in neutral chloride solutions. *Surf. Coat. Technol.* **2004**, *184*, 133–140. [[CrossRef](#)]
53. Ma, L.; Chen, F.; Li, Z.; Gan, M.; Yan, J.; Wei, S.; Bai, Y.; Zeng, J. Preparation and anticorrosion property of poly (2, 3-dimethylaniline) modified by nano-SiO₂. *Compos. Part B Eng.* **2014**, *58*, 54–58. [[CrossRef](#)]
54. Matin, E.; Attar, M.; Ramezanzadeh, B. Investigation of corrosion protection properties of an epoxy nanocomposite loaded with polysiloxane surface modified nanosilica particles on the steel substrate. *Prog. Org. Coat.* **2015**, *78*, 395–403. [[CrossRef](#)]
55. Li, X.; Deng, S.; Fu, H.; Mu, G. Synergistic inhibition effect of rare earth cerium (IV) ion and anionic surfactant on the corrosion of cold rolled steel in H₂SO₄ solution. *Corros. Sci.* **2008**, *50*, 2635–2645. [[CrossRef](#)]
56. Bentiss, F.; Lebrini, M.; Lagrenée, M. Thermodynamic characterization of metal dissolution and inhibitor adsorption processes in mild steel/2, 5-bis (n-thienyl)-1, 3, 4-thiadiazoles/hydrochloric acid system. *Corros. Sci.* **2005**, *47*, 2915–2931. [[CrossRef](#)]
57. Velusamy, S.; Sakthivel, S.; Neelakantan, L.; Sangwai, J.S. Imidazolium-based ionic liquids as an anticorrosive agent for completion fluid design. *J. Earth Sci.* **2017**, *28*, 949–961. [[CrossRef](#)]
58. Eyley, S.; Thielemans, W. Imidazolium grafted cellulose nanocrystals for ion exchange applications. *Chem. Commun.* **2011**, *47*, 4177–4179. [[CrossRef](#)]

Disclaimer/Publisher's Note: The statements, opinions and data contained in all publications are solely those of the individual author(s) and contributor(s) and not of MDPI and/or the editor(s). MDPI and/or the editor(s) disclaim responsibility for any injury to people or property resulting from any ideas, methods, instructions or products referred to in the content.